

# Understanding the Ageing Processes of Electrolytes in Aqueous Magnesium Batteries Using Radiation Chemistry

Malaurie Paillot,<sup>[a, b]</sup> Alan Wong,<sup>[c]</sup> Sergey A. Denisov,<sup>[d]</sup> Jean-Pierre Dognon,<sup>[c]</sup> Mehran Mostafavi,<sup>[d]</sup> Magali Gauthier,<sup>\*[a]</sup> and Sophie Le Caër<sup>\*[b]</sup>

Manufacturing aqueous batteries based on the magnesium cations is an important step towards more sustainable and safer energy storage solutions. Thus, it is important to understand how these systems age and which species are formed throughout numerous charge/discharge cycles. To this end, we have used radiolysis to induce accelerated ageing in concentrated aqueous solutions of magnesium bis(triflimide) Mg(TFSI)<sub>2</sub> (also called “water-in-salt electrolytes” or WISEs). We demonstrate in this work that the degradation products formed,

whether in the gas or liquid phase, are very similar to those formed in concentrated LiTFSI aqueous solutions. In fact, the behavior under ionizing radiation is driven by the anion/water molar ratio regardless of whether the cation is Li<sup>+</sup> or Mg<sup>2+</sup>. This is because both cations are non-reactive, and the bond strengths in the TFSI<sup>-</sup> anion do not vary with the nature of the cation. Reaction mechanisms are proposed to explain the formation of several species under ionizing radiation.

## Introduction

Modern Li-ion batteries contain liquid electrolytes based on a conductive lithium salt dissolved in organic solvents. These organic solvents offer a wide electrochemical stability window (ESW). The battery's operation is made possible by the formation of the so-called “solid-electrolyte interphase” (SEI),<sup>[1,2]</sup> which is conductive to Li<sup>+</sup> ions but electronically insulating, thus preventing any further degradation of the electrolyte. However, organic electrolytes have a high environmental impact due to their toxicity and their manufacturing cost is high. Replacing costly and toxic organic solvents with water could be a potential solution for reducing the environmental impact of batteries, but their energy density is hampered by water's narrow thermodynamic stability window (1.23 V vs. NHE (Normal Hydrogen Electrode)). Moreover, unlike organic solvents, a protective interface does not form in aqueous electro-

lytes due to the high solubility of most ionic compounds in water. Despite these shortcomings, the introduction of the water-in-salt electrolyte (WISE) concept by Suo et al.<sup>[3]</sup> renewed research interest into aqueous lithium batteries. These highly concentrated aqueous electrolytes in fact echo the super-concentrated organic solutions developed by Yamada's group.<sup>[4]</sup> For example, stability windows of up to more than 3 V can be achieved,<sup>[5]</sup> e.g. with LiTFSI (lithium bis(trifluoromethane-sulfonyl)imide : Li[(CF<sub>3</sub>SO<sub>2</sub>)<sub>2</sub>N]). This is mainly due to the absence of uncoordinated water molecules and the successful formation of a protective SEI layer from anion decomposition on the negative electrode, which limits water degradation by the hydrogen evolution reaction (HER).<sup>[3,6]</sup>

The scarcity and geographic localization of lithium resources inhibits large-scale applications of aqueous lithium batteries, which require five times more lithium than conventional electrolytes.<sup>[7]</sup> Switching to multivalent ions for aqueous batteries, such as magnesium, is a more cost-effective and environmentally friendly way of benefiting from the extended window of aqueous electrolytes. The concept of aqueous Mg batteries is a relevant alternative for moving towards greener, more reliable batteries. However, the application and understanding of WISE for aqueous Mg batteries is limited.<sup>[8–10]</sup> The first study from Xu et al.<sup>[8]</sup> proposed a concentrated aqueous electrolyte of 4 m Mg(TFSI)<sub>2</sub> (magnesium bis(trifluoromethane-sulfonyl)imide: Mg[(CF<sub>3</sub>SO<sub>2</sub>)<sub>2</sub>N]<sub>2</sub>), with a potential stability window of 2 V. Subsequently, only a few other studies on aqueous Mg batteries were published based on the molecular crowding approach<sup>[11]</sup> using either a PEG (polyethylene glycol)-Mg(TFSI)<sub>2</sub>-H<sub>2</sub>O<sup>[9]</sup> system or a PVA (poly(vinyl acetate))-Mg(NO<sub>3</sub>)<sub>2</sub>-based aqueous gel electrolyte.<sup>[10]</sup> This only extended the ESW on stainless steel to 2.3 and 2.2 V, respectively.

These rather limited ESW values raise questions about reactivity in Mg-concentrated aqueous solutions. The limited solubility of magnesium salts (up to only 4 to 5 m depending on the salt considered) compared to lithium or potassium salts

[a] M. Paillot, M. Gauthier  
Université Paris-Saclay, CEA, CNRS, NIMBE, LEEL, 91191 Gif-sur-Yvette Cedex, France  
E-mail: magali.gauthier@cea.fr

[b] M. Paillot, S. Le Caër  
Université Paris-Saclay, CEA, CNRS, NIMBE, LIONS, 91191 Gif-sur-Yvette Cedex, France  
E-mail: sophie.le-caer@cea.fr

[c] A. Wong, J.-P. Dognon  
Université Paris-Saclay, CEA, CNRS, NIMBE, LSDRM, 91191 Gif-sur-Yvette Cedex, France

[d] S. A. Denisov, M. Mostafavi  
Institut de Chimie Physique, UMR 8000, CNRS – Université Paris Saclay, Bâtiment 349, 91405 Orsay, France

Supporting information for this article is available on the WWW under <https://doi.org/10.1002/batt.202400209>

© 2024 The Authors. *Batteries & Supercaps* published by Wiley-VCH GmbH. This is an open access article under the terms of the Creative Commons Attribution License, which permits use, distribution and reproduction in any medium, provided the original work is properly cited.

could explain the narrow potential window. However, if one considers the quantity of water, these solutions fulfill the WISE condition, with a quantity of salt greater than that of water, both by mass and volume. As such, one may wonder how the bivalent character of  $Mg^{2+}$  and its affinity for water, which differs from that of lithium,<sup>[5]</sup> influence the water-ion interactions and the hydrogen bond network in Mg-based solutions. Consequently, comprehensive studies of degradation pathways in Mg-based aqueous electrolytes are necessary to understand if and how they depend on the nature of the cation.

Electrolyte degradation studies are time-consuming when assessing the long-term reactivity of cells and, in particular, the electrolytes they contain. We recently demonstrated that radiation chemistry can quickly and efficiently anticipate decomposition pathways in LiTFSI-based aqueous electrolytes.<sup>[12]</sup> This is because radiolysis experiments simulate the reduction and oxidation of electrolytes inside batteries.<sup>[13,14]</sup> More precisely, whether in radiolysis or electrochemistry experiments, the same primary degradation species are initially produced: the electron and the cation radical of the molecule in question. Naturally, these reactions take place within the whole volume of the electrolyte in the case of radiolysis, while the reduction and oxidation reactions take place on electrodes in electrochemical experiments. That said, and despite these differences, the same types of molecules are produced in both experiments. Note that they are not formed in the same quantities, but they are broadly the same molecules, as demonstrated in the case of diethyl carbonate<sup>[15]</sup> or propylene carbonate<sup>[16]</sup> solvents for example. Our aim is here to quickly identify by radiolysis the molecules that can be produced and to use the possibilities offered by pulse radiolysis to gain kinetic information on the transient species formed, which are data inaccessible to battery experiments.

Therefore in this work, we studied the degradation mechanisms of  $Mg(TFSI)_2$ -based aqueous solutions using picosecond pulse radiolysis and the nature of the stable products formed after irradiation. The effect of the salt concentration on degradation pathways was found. Furthermore, the effect of cation change on electrolyte properties and degradation mechanisms is discussed by comparing the LiTFSI and  $Mg(TFSI)_2$  systems.

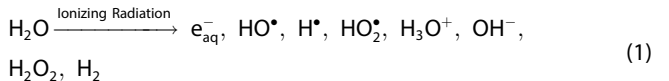
## Results and Discussion

The different  $Mg(TFSI)_2$ /water mixtures are expressed in molality  $m$ , corresponding to the amount of solute ( $n_{\text{salt}}$ ) per kilogram of solvent (water). The maximum amount of  $Mg(TFSI)_2$  that can be dissolved in water at room temperature is limited to 4 m.<sup>[8]</sup> Five solutions from 0.5 m to 3.5 m were chosen to limit possible crystallization. The various characteristics of these mixtures are shown in Table 1. As expected, and as already reported in the case of LiTFSI,<sup>[12]</sup> the density and viscosity (measured at 20 °C) increase with molality. Viscosity values measured at 25 °C have already been reported for  $Mg(TFSI)_2$  solutions.<sup>[17]</sup> These reported viscosity values are lower than our measurements at 20 °C; however, the overall increasing viscosity trend with increasing molality is the same.

In order to understand the degradation processes at work in these solutions, radiolysis experiments were carried out. These experiments provide a better understanding of the first species created by radiation/matter interaction, which are also the first species created electrochemically.

### Picosecond Pulse Radiolysis Experiments

**Radiolysis of water can be written as follows (R1)**<sup>[18]</sup>



Firstly, we conducted picosecond pulse radiolysis experiments to track the species created during the first moments of the radiation/matter interaction. The first species to follow is the solvated electron, for which the absorption spectrum in water is well known (Figure 1a).<sup>[19]</sup> This species is the most important reaction intermediate. It is a precursor of the dihydrogen molecule, which is reported in electrochemical and battery ageing experiments, especially when water reduction occurs. In radiation chemistry, an important parameter is the dose transmitted to the sample. The dose, expressed in Gy (1 Gy = 1 J·kg<sup>-1</sup>), corresponds to the amount of energy deposited in matter per unit of mass. The radiolytic yield, expressed in mol·J<sup>-1</sup>, corresponds to the amount of a species formed (or destroyed) per unit of energy deposited in the matter. It should be noted that, in the liquid phase, the values of these yields are

**Table 1.** Characteristics of the different  $Mg(TFSI)_2$ /water mixtures studied at 20 °C.

Solutions	$Mg(TFSI)_2$ concentration (mol L <sup>-1</sup> )	Ionic strength	H <sub>2</sub> O/Mg <sup>2+</sup> molar ratio	H <sub>2</sub> O/TFSI <sup>-</sup> molar ratio	Mg <sup>2+</sup> /H <sub>2</sub> O weight ratio	wt. % (salt)	wt. % (water)	Density at 293 K (g·cm <sup>-3</sup> )	Dynamic viscosity at 293 K (mPa s)
0.5 m	0.44	1.3	111.1	55.6	0.29	22.6	77.4	1.14	1.6
1 m	0.8	2.4	55.6	27.8	0.58	36.9	63.1	1.25	2.4
2 m	1.3	3.9	27.8	13.9	1.17	53.9	46.1	1.41	4.8
3 m	1.65	5.0	18.5	9.3	1.75	63.7	36.3	1.52	8.5
3.5 m	1.8	5.4	15.9	7.9	2.05	67.2	32.8	1.56	11.0

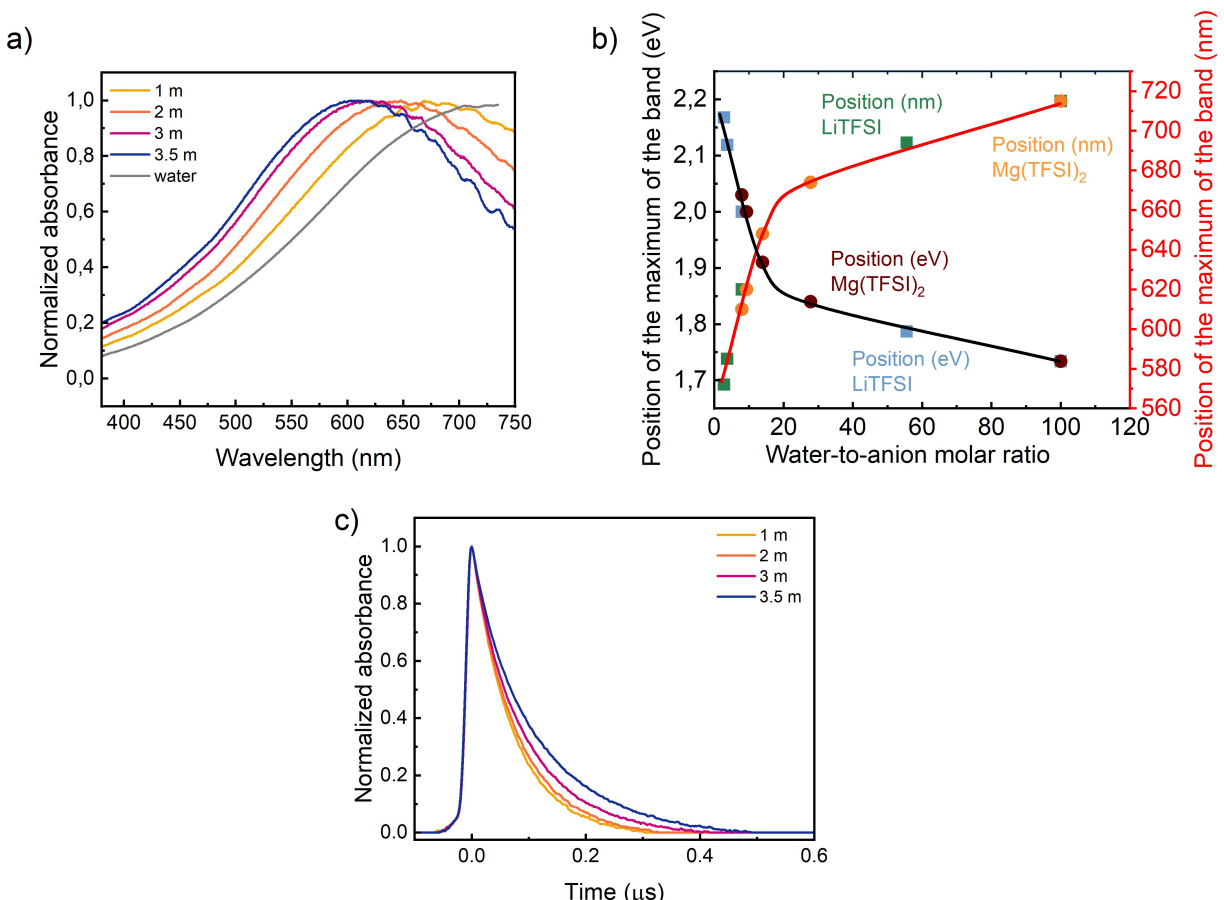


**Figure 1.** a) Normalized absorption spectra of the hydrated electron in pure water and in water/Mg(TFSI)<sub>2</sub> solutions. The molality of the salt is indicated. b) Comparison of the position of the maximum of the spectrum of the solvated electron in the various mixtures, expressed in nm (left axis) or in eV (right axis). The positions obtained in the case of LiTFSI mixtures are also given for the sake of comparison (see reference [12]). The darker colours and circles are used for solutions containing Mg(TFSI)<sub>2</sub>, while the lighter colours and squares are used for solutions containing LiTFSI (see reference<sup>[12]</sup>). For a more relevant comparison between the two salts, we have chosen to express the values as a function of the water-to-anion molar ratio (see Table 1). The lines are a guide for the eyes. c) Normalized decay kinetics of the hydrated electron in various Mg(TFSI)<sub>2</sub>/water mixtures. Measurements were performed at room temperature (293 K), and the dose received by water was 110 Gy per pulse.

not very sensitive to the value of the dose rate, or dose transmitted to the sample per unit time.<sup>[20]</sup>

The normalized absorbance spectra measured for each solution immediately after (10 ps) the radiation/matter interaction are shown in Figure 1a. All spectra have similar shapes regardless of the molality, implying that they can be attributed to the formation of the solvated electron. Moreover, the full width at half-maximum of the absorption band generally remains the same, irrespective of molality. This also implies that the electron's molar absorption coefficient does not change significantly with molality.<sup>[12]</sup> The maximum band position depends on the molality and shifts towards lower wavelengths as the molality increases. This blue shift in the spectrum of the solvated electron in the presence of various salts is well-known in the literature<sup>[21,22]</sup> and corresponds to the pairing of the hydrated electron with non-reactive metal cations such as Mg<sup>2+</sup> or Li<sup>+</sup>.<sup>[21–23]</sup> Mixed quantum/classical simulations have proven that the spectral blue shift is due to the formation of cation/electron contact ion pairs and that the number of contact ion pairs increases with the salt concentration. This explains the enhanced blue shift in

Figure 1a.<sup>[23]</sup> The wavelength shift observed is more pronounced in Mg(TFSI)<sub>2</sub> solutions compared to LiTFSI solutions (Figure 1b). With the same anion, divalent cations induce a larger blue shift of the spectrum of the solvated electron than monovalent cations.<sup>[21]</sup> In the case of multivalent cations, hydrated electrons can simultaneously pair with a larger number of these cations than monovalent cations due to a larger free energy of interaction.<sup>[24]</sup> Lastly, the blue shifts reported here for Mg(TFSI)<sub>2</sub> solutions are similar to those already reported in the case of Mg(ClO<sub>4</sub>)<sub>2</sub>.<sup>[22]</sup> In the case of the perchlorate anion, simulations have evidenced that there is almost no pairing between anions and cations, thus forming cation-electron contact pairs without anions, which in turn explains the extent of the blue shift.<sup>[24]</sup> Therefore, presumably the TFSI<sup>-</sup> anion behaves in the same way as the ClO<sub>4</sub><sup>-</sup> anion.

It should be noted that in the 15 and 20 m LiTFSI solutions, the electron solvation phenomenon occurs with a characteristic time of around fifty picoseconds.<sup>[12]</sup> No such process is observed here in the Mg(TFSI)<sub>2</sub> solutions. The Mg(TFSI)<sub>2</sub> solutions are less viscous (Table 1) than the most concentrated LiTFSI solutions, for which the dynamic viscosity was 25 and 63 mPa s for

molalities of 15 and 20 m, respectively. The difference in dynamic viscosity can explain this discrepancy. In the case of  $\text{Mg}(\text{TFSI})_2$  solutions, electron solvation occurs on time scales that are not experimentally accessible.

The normalized decay kinetics of the solvated electron in the different solutions are shown in Figure 1c on a timescale of a few hundred nanoseconds. The electron decay slows down when raising the salt content, which is certainly due to the viscosity increase with increasing molality (Table 1). The electron decay kinetics are clearly slower in LiTFSI solutions (see Figure S1). Thus, the solvated electron decays more slowly in the solution with 1 m LiTFSI than in a 3.5 m  $\text{Mg}(\text{TFSI})_2$  solution; this is the case even if the dynamic viscosity (1.4 mPa s)<sup>[12]</sup> and the amount of salt (22 wt.% of salt in the sample) are lower in the 1 m LiTFSI solution compared to the magnesium solutions.<sup>[12]</sup> Hence, the solvated electron is more reactive in  $\text{Mg}(\text{TFSI})_2$  solutions than in LiTFSI electrolytes. The evolution of absorbance at time 0 demonstrates that the solvated electrons come not only from the water, but also from the irradiation of the salt. This salt irradiation produces electrons, some of which then solvate into the water (see the corresponding section of the SI with Table S1).

In addition to the solvated electron, another weakly absorbing species in the UV region with a maximum ca. 330 nm was detected by pulse radiolysis (Figure 2a). This spectrum is attributed to the  $\text{TFSI}^{\bullet}$  radical species.<sup>[25]</sup> The signals are weak

and noisy, and their evolution from 10 ns to 160  $\mu\text{s}$  is depicted in Figure 2b-d for two different molalities (1 m and 3.5 m). In all cases, the radicals are formed very quickly after the electron pulse (Figure 2b). The signals remain stable for a few  $\mu\text{s}$  (Figure 2b-d) before decreasing slowly over several hundred microseconds (Figure 2d). This observation implies that this radical reacts slowly. The radical can be formed directly or indirectly. The radical can be directly produced via radiolysis of the salt. This leads to the formation of the electron (which can then solvate), the  $\text{TFSI}^{\bullet}$  radical, and the excited  $\text{TFSI}^{\bullet*}$  species (R2).



Alternatively, the radical can be indirectly produced via the radiolysis of water. This leads to the formation of the  $\text{HO}^{\bullet}$  radical (R1) which can then react with the  $\text{TFSI}^-$  anions to form the  $\text{TFSI}^{\bullet}$  radical<sup>[25]</sup> (R3).



This radical can also be formed by the reaction (R4) between the water cation radical, a species produced immediately after the radiation/water interaction, and the  $\text{TFSI}^-$  anion:

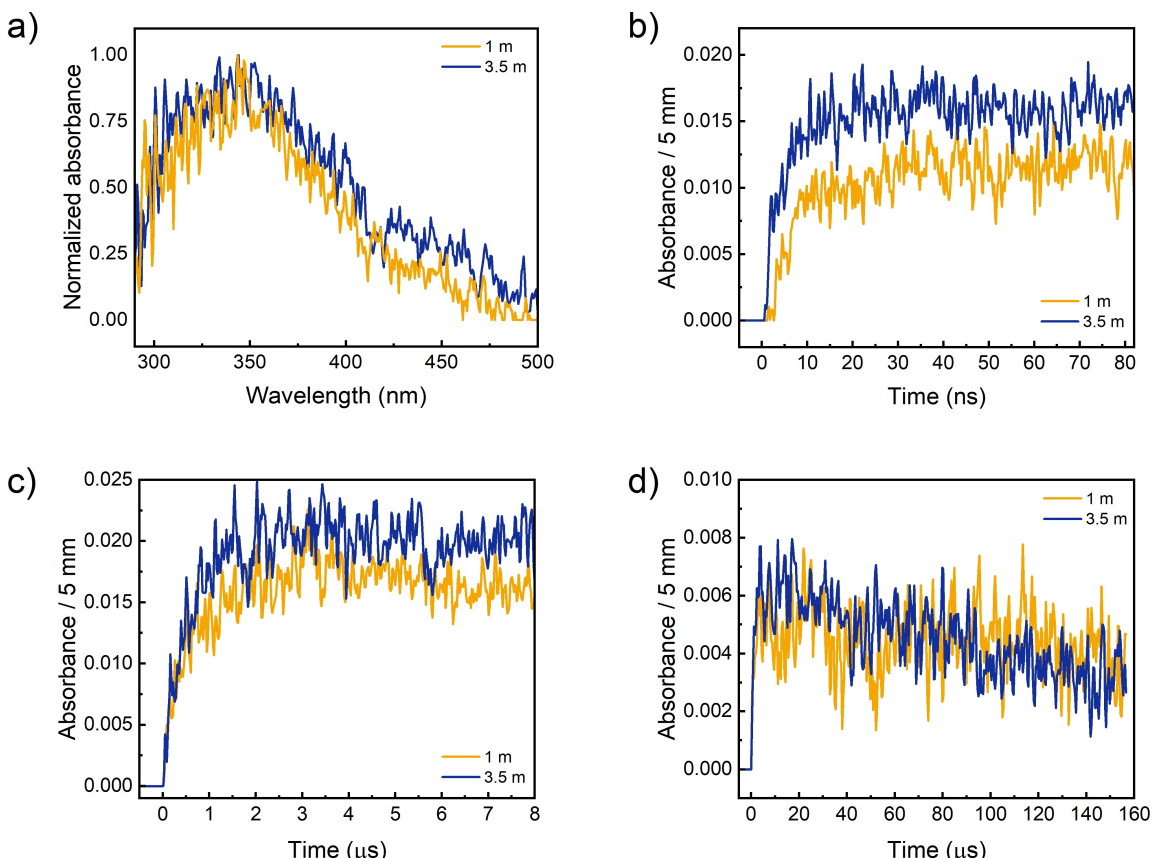


**Figure 2.** (a) Normalized spectrum of the  $\text{TFSI}^{\bullet}$  radical. (b-d) Formation and decay kinetics of the  $\text{TFSI}^{\bullet}$  radical on different timescales for the 1 m and 3.5 m  $\text{Mg}(\text{TFSI})_2$  solutions. Acetone was added to the solution to scavenge the electron. The dose was ca. 50 Gy per pulse.

In these concentrated solutions, the  $\text{H}_2\text{O}^+$  radical can react with either the water or the solute.<sup>[26,27]</sup>

Figures 2b-d show that the intensity of the signals depends little or not at all on the salt content. This implies that these two reaction pathways, which are dependent on water and salt content, are equally effective in producing the TFSI<sup>•</sup> radical. The radical then decreases over long periods of time.

### Production of Stable Molecules Formed in the Gas Phase Upon Irradiation

Radiation chemistry was used to better understand the degradation mechanisms of Mg(TFSI)<sub>2</sub> solutions, particularly as a function of molality. The production of stable molecules after irradiation has been analyzed, particularly in the gas phase, and is discussed in relation to the expected electrochemical degradation. Irradiation of the Mg(TFSI)<sub>2</sub> solutions released H<sub>2</sub> and CO<sub>2</sub> gases, which were detected and quantified by micro-gas chromatography. The quantity of these two gases has been normalized by the corresponding sample mass and is plotted as a function of the dose in Figure 3 for the different molalities studied. It should be noted here that it is difficult to directly correlate a given electrochemical aging with a dose value deposited in the material. In general, significant aging is obtained after irradiation ranging from a few kGy to a few tens of kGy. Figure 3 shows a linear increase in the amount of gas produced with the dose (see Figure 3a for H<sub>2</sub> production and Figure 3b for CO<sub>2</sub> production). The slope of the straight line corresponds to the value of the radiolytic yield (expressed in mol J<sup>-1</sup>); this is the quantity of gas released per energy deposited in the material. The various radiolytic yield values measured are shown in Table S2 (and in Figure 7).

The H<sub>2</sub> released for each Mg(TFSI)<sub>2</sub> solution can only originate from the degradation of the water molecules. This is because no H atom is present in the salt and no dihydrogen was measured after the irradiation of the powder (no water

present). As expected, the amount of H<sub>2</sub> decreases when the molality increases (Figure 3a) because the number of water molecules also decreases. This trend is similar to what is expected from electrochemical profiles<sup>[8]</sup> and H<sub>2</sub> gas measurements on water-in-salt systems.<sup>[28,29]</sup> Note that the radiolysis of pure water does not produce H<sub>2</sub>, as there is a balance between the destruction and the production rate. During the destruction rate process, the OH<sup>•</sup> radical is crucial as it attacks dihydrogen and limits its production.<sup>[20]</sup> In order to detect H<sub>2</sub>, some scavengers of OH<sup>•</sup> radicals are thus used in water. In the Mg(TFSI)<sub>2</sub> aqueous solutions, the salt acts as a scavenger role and promotes, at very low molality, the production of H<sub>2</sub>, as observed above by pulse radiolysis (see reaction R3).<sup>[12]</sup> It is well known that water's primary H<sub>2</sub> radiolytic yield is equal to  $4.5 \times 10^{-8}$  mol J<sup>-1</sup>.<sup>[20]</sup> Noticeably, the value for the 0.5 m Mg(TFSI)<sub>2</sub> electrolyte is higher ( $(7.3 \pm 0.7) \times 10^{-8}$  mol J<sup>-1</sup>) than in pure water; this suggests efficient recombination between two hydrogen atoms and/or two hydrated electrons (see for instance the fast decay of the solvated electron in Figure 1c).

The production of CO<sub>2</sub> increases with molality. This is expected given the amount of carbon increases with molality (from the increase of salt content); thus, the CO<sub>2</sub> production also increases. Unlike LiTFSI powder,<sup>[12]</sup> for which no carbon dioxide production was observed under irradiation, a significant amount of CO<sub>2</sub> is released upon irradiation of the Mg(TFSI)<sub>2</sub> salt, showing that Mg(TFSI)<sub>2</sub> degrades to produce CO<sub>2</sub> itself. In addition, we verified that the Mg(TFSI)<sub>2</sub> salt contained very little water and that even after heat treatment to remove potentially adsorbed water, CO<sub>2</sub> production under ionizing radiation remained the same. That means that CO<sub>2</sub> production is indeed coming from the salt itself, and not from any residual water. The anion's CF<sub>3</sub> bond plays a crucial role as the sole carbon source, while the S=O bond provides the source of oxygen. In solution, both water and the anion can supply oxygen atoms. Once in the water, the oxygen atoms of water are the main source of oxygen atoms for CO<sub>2</sub> production.

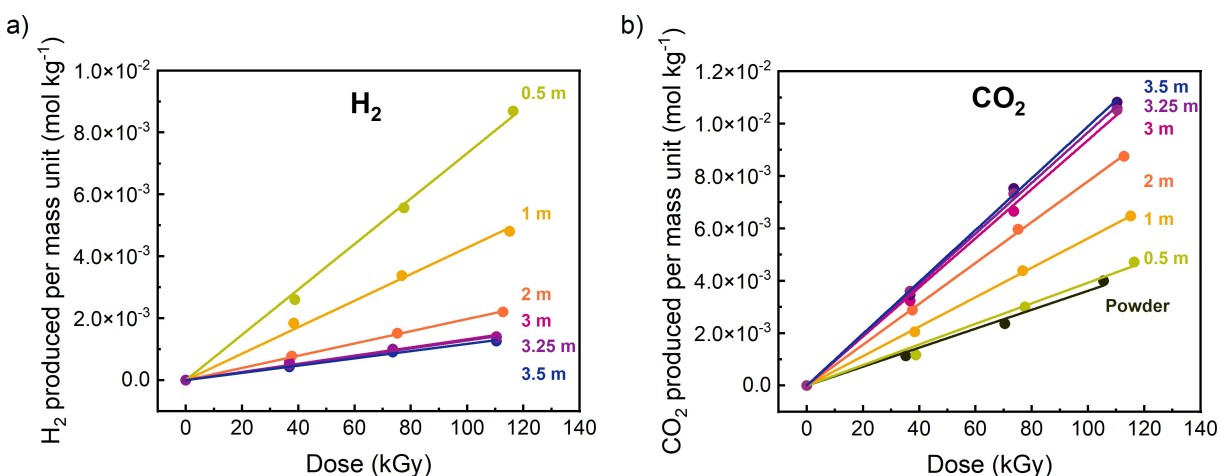


**Figure 3.** Evolution of (a) the amount of H<sub>2</sub> and (b) CO<sub>2</sub> produced per mass unit as a function of the dose for different Mg(TFSI)<sub>2</sub> molalities. The gas production varies linearly with the dose. In each case, the slope of the line gives the gas radiolytic yield. The dose received by the samples was corrected by the F factor on the basis of the dose received in water, as explained in the experimental section.

Globally, the degradation pathways differ at low and high molality. At 0.5 m, the value of the radiolytic yield is higher for H<sub>2</sub> ( $(7.3 \pm 0.7) \times 10^{-8}$  mol J<sup>-1</sup>) compared to CO<sub>2</sub> ( $(3.9 \pm 0.4) \times 10^{-8}$  mol J<sup>-1</sup>), denoting a preferential degradation of water molecules. Whereas at the highest molality, the amount of CO<sub>2</sub> produced is greater than that of H<sub>2</sub>, indicating a preferential attack on the anion. Note that in the case of concentrated solutions, a significant proportion of the radiation is absorbed by the salt itself, which influences the degradation routes. However, the salt molecules are also present on and near the electrodes surface in the electrochemical measurements, and are therefore affecting the degradation mechanisms at the electrode surface. Some studies on LiTFSI solutions have demonstrated that the salt is in fact playing a huge role in the interface's nature.<sup>[6,30]</sup> Consequently, we expect that similar reactive species coming from the salt will be created both in the radiolysis experiments and in electrochemical experiments.

To better understand the degradation mechanisms of aqueous solutions of Mg(TFSI)<sub>2</sub> solutions and the impact of molality on species production, other gases formed under irradiation were identified using gas chromatography coupled to mass spectrometry. These experiments were carried out after irradiating the powder itself and two solutions containing Mg(TFSI)<sub>2</sub> (Figures 4 and S2), with a molality of 1 m and 3 m, respectively. The intensity of each peak was normalized by the mass of the sample, and the area of the peak was proportional to the concentration of the gas detected. The retention times of the gases observed are presented in Tables S3–S5.

A wide variety of gases were detected from the irradiated aqueous solutions. Interestingly, unlike LiTFSI,<sup>[12]</sup> gases were also observed from the powder (Figure 4). Overall, the chromatograms show that a greater quantity of gases and more types of gases are produced in the most concentrated solution. Regardless of whether the molality is low or high, the gases generated in the solutions are often composed of -CF<sub>3</sub> derivatives, suggesting a preferential cleavage of the C–S bond of the anion in these electrolytes. Only one hydrogen-containing species, CHF<sub>3</sub>, was produced. Therefore, at low molality, degradation is induced by the presence of water with the production of H<sub>2</sub> (Figure 3) and CHF<sub>3</sub>, but the anion also has a significant impact with many species observed possessing -CF<sub>3</sub> groups. Certain gases, such as SO<sub>2</sub>, C<sub>3</sub>F<sub>8</sub> or C<sub>2</sub>F<sub>5</sub>N, are only present at the highest molality. This indicates a degradation of the TFSI<sup>-</sup> anion for the 3 m molality solution and shows how the high salt concentration affects the reaction pathways. It should also be noted that a significant proportion of the CF<sub>3</sub>-containing species found in the irradiated 3 m solution are present after irradiation of the salt. During the degradation process, the C–S bond is broken which results in the formation of a highly reactive •CF<sub>3</sub> radical. Two of these radicals can form C<sub>2</sub>F<sub>6</sub> or react with the surrounding environment to form different stable species, such as COS from the S=O bonds or C<sub>2</sub>F<sub>5</sub>N from the nitrogen part of the molecule. Note that more COS is formed from the irradiated 1 m solution (Figure 4), suggesting that the oxygen atom in the COS compound comes from a water molecule.

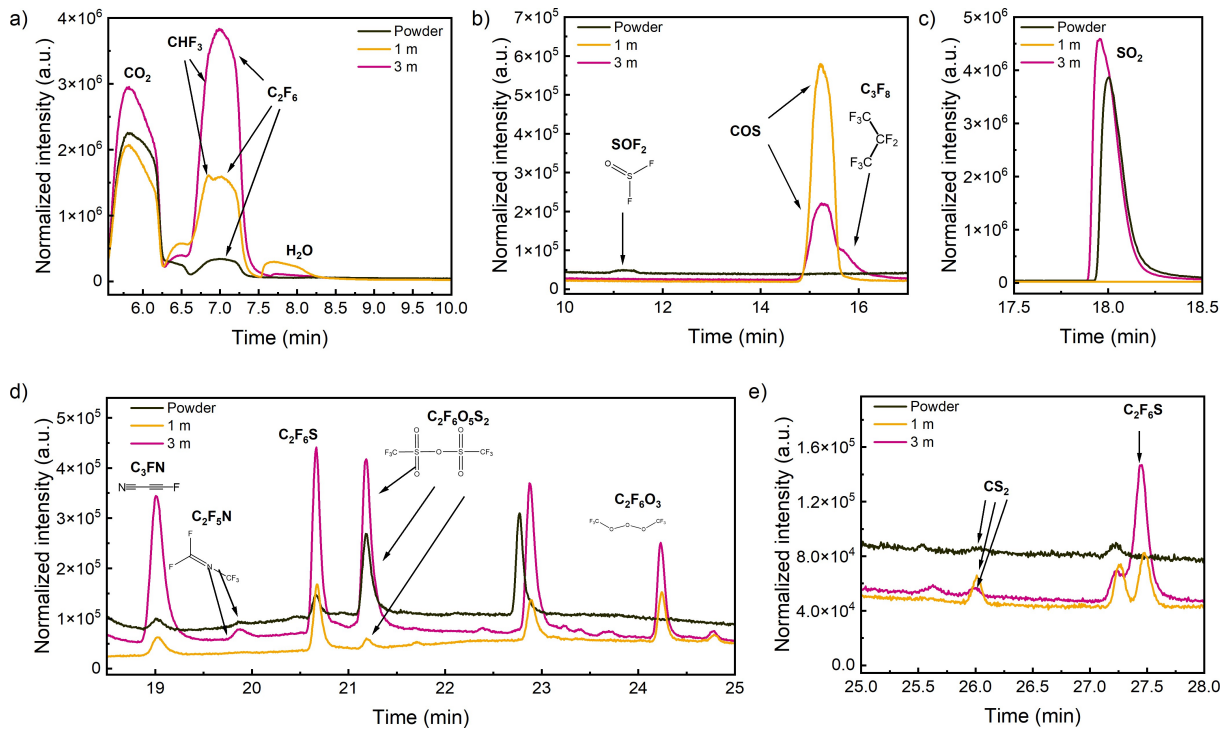


**Figure 4.** GC-MS chromatograms of gases produced after a  $110 \pm 5$  kGy electron irradiation of the Mg(TFSI)<sub>2</sub> powder, 1 m and 3 m Mg(TFSI)<sub>2</sub> aqueous solutions. The species identified are indicated in the figures. (a), (b), (c), (d), and (e) figures correspond to magnified views of some regions of interest (Figure S2 in Supporting Information). The intensity of each peak was normalized by the mass of the sample. For each peak, the area is proportional to the concentration of the corresponding detected molecule. The dose received by the samples was corrected by the F factor based on the dose received in water, as explained in the experimental section.

Moreover, irradiation of the powder alone does not lead to the production of COS. Irradiation of the powder leads to a specific species,  $\text{SOF}_2$ , which is not detected in the solutions after irradiation. This compound indicates that the C–F bonds are broken under these conditions. In addition, the color of the salt changed from white to brownish after irradiation. The absorption spectra (Figures S3–S4) suggest the formation of magnesium metal clusters (observed at 600–800 nm) and  $\text{Mg}^+$  species (observed at around 400 nm<sup>[31]</sup>) in the irradiated  $\text{Mg}(\text{TFSI})_2$  powder (see SI for more details).

After the gas phase, analysis of the liquid phase by NMR spectroscopy also highlights the degradation of the salt (Figure 5 and Table S6 for peaks assignments).  $^{19}\text{F}$  and  $^1\text{H}$  NMR were performed to identify the liquid degradation products obtained in a 3 m  $\text{Mg}(\text{TFSI})_2$  solution after a 500 kGy irradiation dose. A wide range of low-intensity compounds were detected in the fluorine spectrum between 60 and –200 ppm (Figure 5a). The main products are located around the  $\text{TFSI}^-$  signal (–78.3 ppm) in the –90 to –60 ppm range and are derived from the reactivity of the sulfonic and  $-\text{CF}_3$  groups, such as  $\text{CF}_3\text{SO}_2\text{NH}_2$ ,  $\text{CF}_3\text{SO}_3\text{CH}_3$  or  $\text{CF}_3\text{SOOH}$ . Between 20 and 60 ppm, species such as  $\text{R}-\text{S}(\text{O})_x\text{F}_y$  are also detected in small quantities. The shielded region of the spectrum below –120 ppm shows some characteristic signals from  $\text{HF}_2^-$  (–144.2 ppm) and HF (–148.7 ppm), as well as some  $\text{MgF}_2$  (–123.9 ppm).

The  $^{19}\text{F}$  doublet at –122.2 ppm (Figure 5c) and the  $^1\text{H}$  triplet signal at 6.7 ppm (Figure 5c) indicate the presence of fluorinated alkyl compounds  $\text{R}-\text{CF}_2\text{H}$ . The  $^1\text{H}$  spectrum (Figure 5b)

also corroborates the presence of HF (8.2 ppm) and suggests the presence of a  $\text{CF}_3\text{SO}_2\text{OH}$  species (7.3 ppm) derived from sulfuric acid.

The nature of the species formed corresponds reasonably well to the composition of the compounds found during irradiation of aqueous LiTFSI solutions (see Figure S5), particularly for the 7 m LiTFSI solution, which has a similar water content.<sup>[12]</sup>

## Discussion

Some of the reactions describing the behavior of these electrolytes under ageing are depicted in Figure 6. Reactions taking place in water alone are shown in the blue box, reactions occurring in salt are shown in the orange box, and reactions occurring from species from both water and salt are noted in the grey box. The species involved in the radiolysis of water are well known, and water radiolysis involves in particular the formation of  $\text{HO}^\bullet$ , the solvated electron and the hydrogen atom (blue box<sup>[18]</sup>). In addition, the radiolysis of ionic liquids involving the  $\text{TFSI}^-$  anion has already been the subject of detailed work.<sup>[32–35]</sup> We therefore rely on the intermediates described in these articles to propose the mechanism below. A more detailed discussion of these mechanisms can be found in.<sup>[12]</sup>

Based on the  $\text{H}_2$  and  $\text{CO}_2$  production, radiolytic yield values can be discussed not in terms of molality, but as a function of

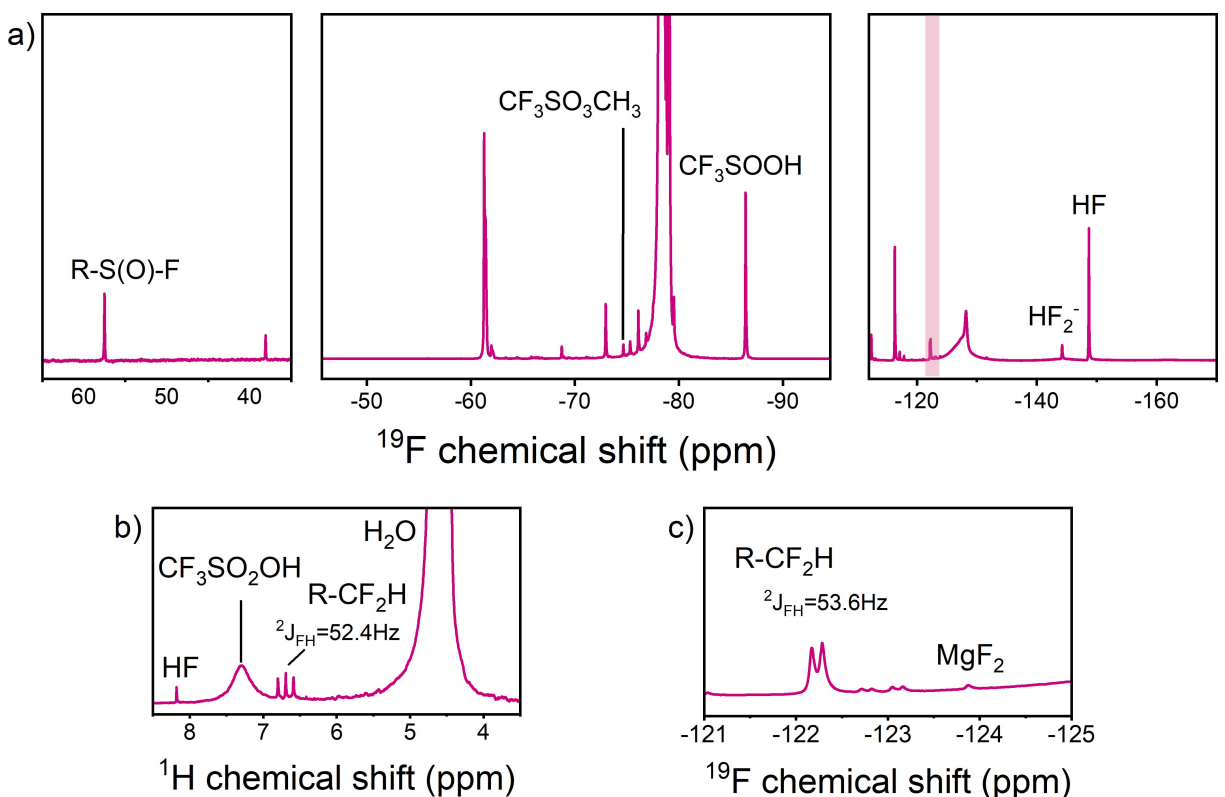


**Figure 5.** a)  $^{19}\text{F}$  and b)  $^1\text{H}$  NMR spectra of the 3 m  $\text{Mg}(\text{TFSI})_2$  aqueous solution irradiated at 500 kGy. c) Magnified view of the pink region of the  $^{19}\text{F}$  spectrum in a).

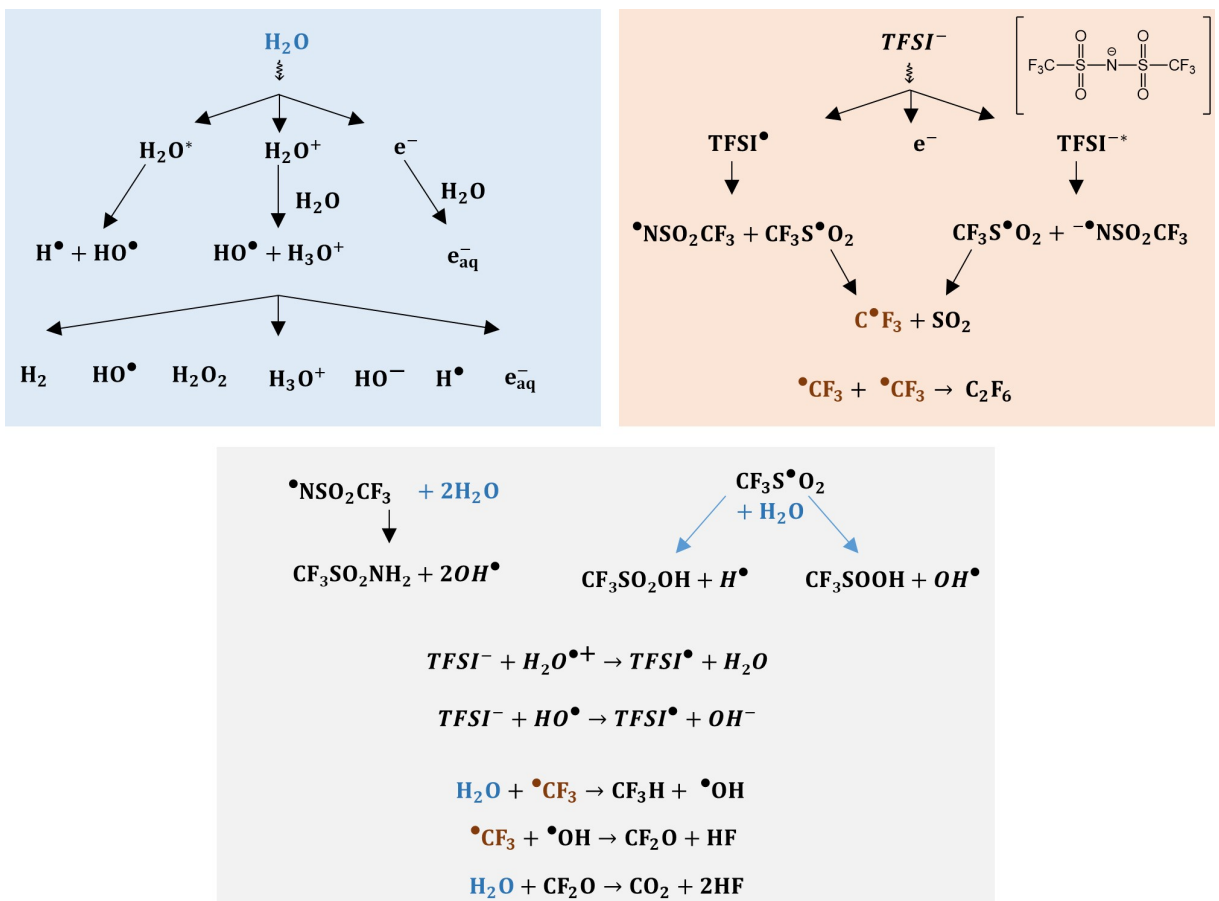


**Figure 6.** Possible reaction pathways taking place in the irradiated  $\text{Mg}(\text{TFSI})_2$  concentrated aqueous electrolyte. The reaction routes of the water radiolysis are given in the blue box and the pathways of the anion  $\text{TFSI}^-$  are only in the orange box. Reactions between the water and the species of the anion reactions are given in the grey box.

the molar ratio between water and anion in the solution (see Table 1). Figure 7 shows the evolution of these radiolytic yields as a function of the molar ratio of the samples. The values

obtained for solutions containing LiTFSI have also been plotted for comparison.<sup>[12]</sup> The water/anion ratio is, in fact, a more relevant parameter when comparing solutions containing

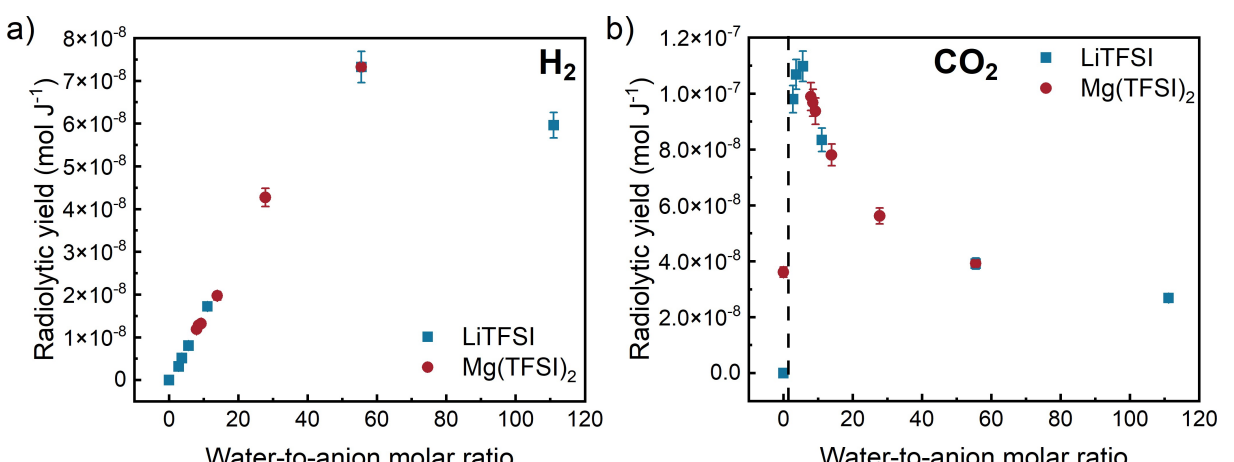


**Figure 7.** Evolution of the (a)  $\text{H}_2$  and (b)  $\text{CO}_2$  radiolytic yields as a function of the water-to-anion molar ratio for LiTFSI (blue squares) and  $\text{Mg}(\text{TFSI})_2$  (brown circles)-based aqueous solutions. The point acquired at a molar ratio of 0 corresponds to the irradiated  $\text{Mg}(\text{TFSI})_2$  powder. The radiolytic yields measured in the LiTFSI solutions come from reference [12]. In all cases, the dose received by the samples was corrected by the F factor on the basis of the dose received in water, as explained in the experimental section. The data from reference<sup>[12]</sup> were thus also corrected from their corresponding F factor.

monovalent or multivalent cations since, for a similar molality, the anion content is twice as high in the  $Mg^{2+}$  system as in the  $Li^+$  system. The production of  $H_2$  and  $CO_2$  follows the same trends and values regardless of whether the salt is LiTFSI or  $Mg(TFSI)_2$ . Of course, as LiTFSI is more soluble than  $Mg(TFSI)_2$ , the accessible range of salt content values is greater than in the case of  $Mg(TFSI)_2$ . The trend observed suggests that the organization of water and ions in the solutions is similar for a constant anion content and that the monovalent or bivalent character of the cation does not greatly affect the solution or its reactivity. This behavior is observed also because neither  $Li^+$  nor  $Mg^{2+}$  are reactive under radiolysis. However, a major difference comes from the behavior of the powder alone in the absence of water, since  $Mg(TFSI)_2$  produces  $CO_2$  under irradiation, unlike LiTFSI (Figure 7b), as indicated above.

In the case of  $H_2$ , the general trend is a decrease in  $H_2$  production as the salt fraction increases (Figure 7a), after an initial increase (linked to competition between  $H_2$  production from water and the presence of salt, which protects  $H_2$  from attack by  $HO^\bullet$  radicals). This is expected since  $H_2$  comes from water for which the mass fraction decreases with increasing salt fraction (Table 1). The evolution of the radiolytic yield of  $CO_2$  with increasing salt content mirrors that of  $H_2$ . That is, the yield increases with the amount of salt. This is expected since the only source of carbon comes from the salt. However,  $CO_2$  yield decreases at the highest salt mass fractions, due to the decreasing fraction of water which is the source of oxygen atoms.

The absence of a strong effect of the mono- or bivalent character of the cation can be rationalized by considering the nature of the bonds within the  $TFSI^-$  anions. To compare chemical bond strengths in  $TFSI^-$  anions for Li and Mg compounds (see Figure S6), we performed quantum chemical calculations using the ORCA software package<sup>[36]</sup> (see the Experimental section for details). We included 10 and 20 water molecules in the lithium and magnesium compounds respectively to account for the presence of water in the electrolyte (Figure S6). Recently, the Intrinsic Bond Strength Index (IBSI) has been proposed as a new tool for evaluating the strength of any bond.<sup>[37]</sup> IBSI is a dimensionless value that does not correspond to a bond order but reflects the bond strength. In this work, it was used in the context of a Hirshfeld partition as implemented in the Multiwfn software.<sup>[38]</sup>

Table S7 shows that the bond strengths in  $TFSI^-$  anions are not very sensitive to the environment and are globally the same for the LiTFSI and  $Mg(TFSI)_2$  compounds. However, due to the different coordination of  $Li^+$  and  $Mg^{2+}$  ions in solution (Figure S6), the IBSI value for the non-covalent interaction of M–O is different and is weaker for  $Li^+...O$  than for  $Mg^{2+}...O$  (see Table S7). The stability of the cation- $TFSI^-$  complex is mainly governed by electrostatic interaction without large electron density perturbations (see Figure S7). These results explain why degradation products are formed in the same quantities, for a given anion/water molar ratio, regardless of the nature of the cation.

The results obtained in the case of the salt alone are different for  $Mg(TFSI)_2$  compared to LiTFSI (Figure 7b). For

instance, there is  $CO_2$  production observed in irradiated  $Mg(TFSI)_2$  unlike in irradiated LiTFSI. However, in the presence of water molecules, IBSI indices show that bond strengths are the same in the anion, whether the cation is  $Li^+$  or  $Mg^{2+}$ . An explanation can then be found in the structure of the compounds. Indeed, the molecular arrangements of LiTFSI and  $Mg(TFSI)_2$  in the solid phase are different, as shown in Figure S8. In LiTFSI, structural integrity is ensured by  $Li-O-Li$  bridges (Figure S8), which are not present in  $Mg(TFSI)_2$ .  $Li-Li$  distances are in the order of 3.22 Å in LiTFSI compared to 9.24 Å for Mg–Mg distances in  $Mg(TFSI)_2$ . It can then be assumed that the bonds cleaved by ionizing radiation will reform in the lithium salt, but not in the magnesium salt. This leads to the formation of products in the case of magnesium, but not for lithium.

## Conclusions

In this work, we have elucidated the main degradation mechanisms of concentrated  $Mg(TFSI)_2$  aqueous solutions induced by ionizing radiation, which mimics the aging induced by repeated charging and discharging cycles in aqueous batteries.

We used picosecond pulsed radiolysis to evidence the formation of the solvated electron, whose transient absorption spectrum becomes increasingly blue-shifted as the molality of the salt increases. These pulsed radiolysis experiments also showed the formation of  $TFSI^\bullet$  radicals, which are formed by attack of the hydroxyl radical or of the water cation radical on the  $TFSI^-$  anion. These radicals were observed on time scales of over 100 μs, testifying to low reactivity.

Concerning the production of stable molecules,  $H_2$  and  $CO_2$  were quantified. The  $H_2$  radiolytic yield decreases with increasing molality, due to decreasing water content. Conversely, the  $CO_2$  radiolytic yield increases with increasing molality as it originates from the degradation of the anion. Other gases such as  $SO_2$ ,  $COS$ , and compounds containing the  $-CF_3$  group were also detected by gas chromatography coupled to mass spectrometry. They are formed in greater quantities, and the number of species detected is greater as the molality increases. Other degradation products formed in the liquid phase were also identified by  $^{19}F$  and  $^1H$  NMR spectroscopy. Reaction mechanisms were proposed to account for a number of species formed under ionizing radiation.

Finally, the degradation products (and, when possible, their respective quantities) were compared in the case of irradiated LiTFSI and  $Mg(TFSI)_2$  solutions. Clearly, the cation does not play a significant role, and the anion/water (or water/anion) molar ratio controls the quantity and nature of the products formed. This is explained by the fact that the  $Li^+$  and  $Mg^{2+}$  cations are not reactive towards ionizing radiation. Furthermore, quantum chemical calculations have shown that bond strengths are the same in the  $TFSI^-$  anion, regardless of the nature of the cation. This confirms that the cation has a small effect in the degradation routes of these aqueous solutions.

The main difference lies in the degradation products formed in the solid alone under irradiation. Irradiating the Mg(TFSI)<sub>2</sub> salt leads to the formation of CO<sub>2</sub>, unlike LiTFSI, for which no gaseous products were detected. The difference between these two systems cannot be explained by a difference in bond strength within the anion. The crystalline structure of each salt is probably the underlying cause of such a difference.

Overall, we gathered, with an accelerated strategy, valuable insights on the degradation routes of concentrated aqueous electrolytes. We demonstrated the critical importance of the anion/water ratio in comparison to the cation's nature. This work highlights the interest in radiolysis for rapidly probing electrolyte ageing in aqueous batteries.

## Experimental Section

### Electrolyte Preparation and Properties

Magnesium bis(trifluoromethanesulfonyl)imide (Mg[(CF<sub>3</sub>SO<sub>2</sub>)<sub>2</sub>N]<sub>2</sub>, 99.5%, Solvionic) was used as received and stored in a glovebox under argon. The various aqueous solutions were prepared by mixing the salt powder, accurately weighed beforehand in the glove box, with ultrapure water and stirring for 30 minutes at room temperature to solubilize all the salt. Different solutions were made until the solubility limit was reached: 0.5 m, 1 m, 2 m, 3 m and 3.5 m.

The viscosity and the density were performed using a capillary of 1.59 mm diameter in a vibrating-tube densitometer (DMA 4500 M, Anton Parr) coupled to a rolling ball microviscosimeter (Lovis 2000 ME) at 20 °C.

### Radiolysis Experiments for the Detection of the Stable Products Formed

For the irradiation, each sample containing around 1 mL for the liquid, and 1 g for the powder, was placed into a Pyrex glass ampoule (~10 mL). The sample was degassed by bubbling argon for 20 minutes. Then the ampoule was degassed and placed under a pressure of 1.6 bar of ultra-pure argon (99.9999%). The degassing procedure was repeated thrice to remove any air before the irradiation.

The solutions were irradiated using 10 MeV electron pulses produced by a Titan Beta, Inc. linear accelerator (ALIENOR). The experiment conditions were a pulse duration of 10 ns and a repetition range between 2 and 10 Hz. The dose per pulse was measured with Fricke dosimetry.<sup>[39]</sup> It was measured precisely and around 20 Gy per pulse, with 1 Gy = 1 J·kg<sup>-1</sup>.

### Identification of the Products Formed Upon Irradiation in the Gas Phase

The identification and the quantification of H<sub>2</sub>, CH<sub>4</sub>, CO and CO<sub>2</sub>, if any, was performed with a micro-gas chromatography ( $\mu$ -GC-R3000, SRA instrument) with ultra-high purity argon (99.9999%). To measure the radiolytic yield (in mol·J<sup>-1</sup>), the gas was quantified after each irradiation step of around 40 kGy, for a final dose of around 120 kGy. The measurements were systematically reproduced several times in order to assess the uncertainty in gas production. We found a maximum uncertainty of 10%.

Several types of gases were also identified using gas chromatography coupled to mass spectrometry (GC-MS, Agilent Technologies 6890B). The equipment was cleaned between each measurement with argon. The mass spectrometer consists of an electron impact source and a quadrupole mass analyzer. The vector gas used was helium with a 2 mL min<sup>-1</sup> flow rate. The mass range was 4–160. Separation was performed with a CP-PorabondQ (25 m, Ø 0.32 mm) column (Varian). The injector was used at 110 °C in splitless mode.

### NMR Experiments

The <sup>1</sup>H and <sup>19</sup>F NMR experiments on the irradiated samples were carried out on a Bruker 500 MHz NEO operating at a frequency of 499.167 and 469.647 MHz, respectively, with a 4-mm HX magic-angle probe. The <sup>1</sup>H and <sup>19</sup>F spectra were acquired with a single-pulse experiment using a 90° pulse of 4 and 6.25  $\mu$ s, respectively, with a recycle delay of 5 s for a total of 128 transients. The magic angle sample spinning rate was set at 8 kHz. The <sup>1</sup>H and <sup>19</sup>F spectral chemical shifts were referenced to 4.8 ppm of pure H<sub>2</sub>O and -122 ppm of Teflon,<sup>[40]</sup> respectively.

### Picosecond Pulse Radiolysis Experiments

Picosecond pulse radiolysis experiments were conducted at the laser-driven electron accelerator ELYSE at Université Paris-Saclay. The different electrolyte solutions were bubbled with argon to prevent any water uptake during the measurements. Electron pulses with a pulse duration of about 7 ps and an electron energy of 7.6 MeV were provided at a repetition rate of 5 Hz. Depending on the investigated timescale, we used two different experimental configurations. We probed the transient absorbance of the solution with a flow cell with a 5 mm optical path collinear to the electron pulse propagation. The basic optical configuration for this first experimental configuration is a pump-probe setup, which acquires signals up to 10 ns, in the present study 350–720 nm spectral range. Experimental specifications regarding this setup are detailed in reference.<sup>[41]</sup> In the second configuration, signals were measured in the ns- $\mu$ s time scale using a streak camera and a homemade repetitive flash lamp. For one experiment, the acquisition was done in the 300–800 nm wavelength range, at given times and kinetics, and at various wavelengths. The precision of the measurements was around 2 mO.D. (O.D. corresponding to Optical Density).

The absorbance of the hydrated electron e<sup>-</sup><sub>aq</sub> in water gives access to the dose per pulse. It was recorded just before a series of measurements, as explained in reference.<sup>[41]</sup> The dose per pulse in water was very stable throughout the experiments and was about 100 Gy (1 Gy = 1 J·kg<sup>-1</sup>). In the concentrated aqueous electrolytes, the dose factor *F* between the concentrated solutions studied herein and a pure water sample can be calculated using the following equation:

$$F = \frac{\left( \frac{Z_{salt}}{A_{salt}} p + \frac{Z_{water}}{A_{water}} (100 - p) \right)}{\frac{Z_{water}}{A_{water}} 100}$$

with Z<sub>salt</sub> (Z<sub>water</sub>) the number of electrons of Mg(TFSI)<sub>2</sub> and of water respectively; A<sub>salt</sub> (A<sub>water</sub>) the mass number of Mg(TFSI)<sub>2</sub> and of water, respectively, and *p* the weight fraction of the salt, which is presented in Table 1. Here, Z<sub>water</sub> = 10; Z<sub>salt</sub> = 286; A<sub>water</sub> = 18 and A<sub>salt</sub> = 584. When molality increases from 0.5 m to 3.5 m, *F* decreases from 0.97 to 0.92. In the case of the salt alone, *F* = 0.88.

### Spectro-Kinetic Data Analysis

The spectro-kinetics matrix is composed of the absorbance values acquired at different times and wavelengths. The data were corrected with a wavelength-dependent baseline before a multi-variate curve resolution alternating least squares (MCR-ALS) analysis was applied by the spectro-kinetic analysis code (SK-Ana).<sup>[35,36]</sup> We used singular value decomposition to determine the number of absorbing species in a global matrix. We set positivity constraints for both kinetics and spectra.

### Quantum Chemistry Calculations

#### Geometry Optimization

Initial Li(TFSI)(H<sub>2</sub>O)<sub>10</sub> and Mg(TFSI)<sub>2</sub>(H<sub>2</sub>O)<sub>20</sub> configurations were generated using the PACKMOL package.<sup>[44]</sup> The geometry optimizations were performed for initial configurations with the r<sup>2</sup>SCAN-3c<sup>[45]</sup> composite density functional theory (DFT) method using the ORCA 5.0.4 program.<sup>[36]</sup> The approach combines the r<sup>2</sup>SCAN meta-generalized-gradient approximation with triple-ζ Gaussian basis set and the semi-classical D4 and gCP correction potentials for London-dispersion and basis set superposition error.

#### Post-Process, Analysis, and Visualization of Results from ORCA

All r<sup>2</sup>SCAN-3c calculations were analyzed by using Multiwfn (development version 3.8) software.<sup>[38]</sup> The intrinsic bond strength index (IBSI) was computed using IGMH based on Hirshfeld partition of molecular density.

### Acknowledgements

The French EMIR&A network and Jean-Philippe Larbre are gratefully acknowledged for providing irradiation beam time at the ELYSE platform. The authors gratefully acknowledge the French EMIR&A network and Jorge Vieira for providing irradiation beam time and support at ALIENOR platform, respectively. The authors are thankful to Bénédicte Montigny (PCM2E, Tours, France), for support in the density and viscosity measurements and to Taren Cataldo (UNSW, Sydney, Australia) for the thorough reading of the manuscript. This work was supported by the French National Research Agency (ANR) under Project ANR-21-CE50-0005-01. M. P., M. G., and S. L.C would like to thank CEA for funding the Ph.D. of M. P.

### Conflict of Interests

The authors declare no conflict of interest.

### Data Availability Statement

The data that support the findings of this study are openly available in ZENODO at 10.5281/zenodo.10893653, reference number 10893653.

**Keywords:** WISEs • magnesium • energy conversion • degradation mechanisms • radiolysis

- [1] E. Peled, *J. Electrochem. Soc.* **1979**, *126*, 2047–2051.
- [2] M. Gauthier, T. J. Carney, A. Grimaud, L. Giordano, N. Pour, H.-H. Chang, D. P. Fenning, S. F. Lux, O. Paschos, C. Bauer, F. Maglia, S. Lupart, P. Lamp, Y. Shao-Horn, *J. Phys. Chem. Lett.* **2015**, *6*, 4653–4672.
- [3] L. Suo, O. Borodin, T. Gao, M. Olguin, J. Ho, X. Fan, C. Luo, C. Wang, K. Xu, *Science* **2015**, *350*, 938–943.
- [4] Y. Yamada, J. Wang, S. Ko, E. Watanabe, A. Yamada, *Nat. Energy* **2019**, *4*, 269–280.
- [5] J. Han, A. Mariani, S. Passerini, A. Varzi, *Energy Environ. Sci.* **2023**, *16*, 1480–1501.
- [6] N. Dubouis, P. Lemaire, B. Mirvaux, E. Salager, M. Deschamps, A. Grimaud, *Energy Environ. Sci.* **2018**, *11*, 3491–3499.
- [7] M. R. Lukatskaya, J. I. Feldblum, D. G. Mackanic, F. Lissel, D. L. Michels, Y. Cui, Z. Bao, *Energy Environ. Sci.* **2018**, *11*, 2876–2883.
- [8] F. Wang, X. Fan, T. Gao, W. Sun, Z. Ma, C. Yang, F. Han, K. Xu, C. Wang, *ACS Cent. Sci.* **2017**, *3*, 1121–1128.
- [9] Q. Fu, X. Wu, X. Luo, S. Indris, A. Sarapulova, M. Bauer, Z. Wang, M. Knapp, H. Ehrenberg, Y. Wei, S. Dsoke, *Adv. Funct. Mater.* **2022**, *32*, 2110674.
- [10] X. Tang, D. Zhou, B. Zhang, S. Wang, P. Li, H. Liu, X. Guo, P. Jaumaux, X. Gao, Y. Fu, C. Wang, C. Wang, G. Wang, *Nat. Commun.* **2021**, *12*, 2857.
- [11] J. Xie, Z. Liang, Y.-C. Lu, *Nat. Mater.* **2020**, *19*, 1006–1011.
- [12] M. Paillot, A. Wong, S. A. Denisov, P. Soudan, P. Poizot, B. Montigny, M. Mostafavi, M. Gauthier, S. Le Caér, *ChemSusChem* **2023**, *16*, e202300692.
- [13] Y. Levieux-Souid, J.-F. Martin, P. Moreau, N. Herlin-Boime, S. Le Caér, *Small Methods* **2022**, *6*, 2200712.
- [14] D. Ortiz, V. Steinmetz, D. Durand, S. Legand, V. Dauvois, P. Maître, S. Le Caér, *Nat. Commun.* **2015**, *6*, 6950.
- [15] D. Ortiz, I. Jiménez Gordon, J.-P. Baltaze, O. Hernandez-Alba, S. Legand, V. Dauvois, G. Si Larbi, U. Schmidhammer, J.-L. Marignier, J.-F. Martin, J. Belloni, M. Mostafavi, S. Le Caér, *ChemSusChem* **2015**, *8*, 3605–3616.
- [16] D. Ortiz, I. Jimenez Gordon, S. Legand, V. Dauvois, J.-P. Baltaze, J.-L. Marignier, J.-F. Martin, J. Belloni, M. Mostafavi, S. Le Caér, *J. Power Sources* **2016**, *326*, 285–295.
- [17] Z. Yu, T. R. Juran, X. Liu, K. S. Han, H. Wang, K. T. Mueller, L. Ma, K. Xu, T. Li, L. A. Curtiss, L. Cheng, *Energy Environ. Mater.* **2022**, *5*, 295–304.
- [18] S. Le Caér, *Water* **2011**, *3*, 235–253.
- [19] F. Torché, J.-L. Marignier, *J. Phys. Chem. B* **2016**, *120*, 7201–7206.
- [20] J. W. T. Spinks, R. J. Woods, *New York USA by Wiley* **1990**.
- [21] J. Bonin, I. Lampre, B. Soroushian, M. Mostafavi, *J. Phys. Chem. A* **2004**, *108*, 6817–6819.
- [22] J. Bonin, I. Lampre, M. Mostafavi, *Radiat. Phys. Chem.* **2005**, *74*, 288–296.
- [23] W. A. Narvaez, S. J. Park, B. J. Schwartz, *J. Phys. Chem. B* **2022**, *126*, 3748–3757.
- [24] W. A. Narvaez, S. J. Park, B. J. Schwartz, *J. Phys. Chem. B* **2022**, *126*, 7701–7708.
- [25] D. Behar, P. Neta, C. Schultheisz, *J. Phys. Chem. A* **2002**, *106*, 3139–3147.
- [26] J. Ma, U. Schmidhammer, P. Pernot, M. Mostafavi, *J. Phys. Chem. Lett.* **2014**, *5*, 258–261.
- [27] A. K. El Omar, U. Schmidhammer, B. Rousseau, J. LaVerne, M. Mostafavi, *J. Phys. Chem. A* **2012**, *116*, 11509–11518.
- [28] L. Droguet, A. Grimaud, O. Fontaine, J.-M. Tarascon, *Adv. Energy Mater.* **2020**, *10*, 202002440.
- [29] L. Suo, D. Oh, Y. Lin, Z. Zhuo, O. Borodin, T. Gao, F. Wang, A. Kushner, Z. Wang, H.-C. Kim, Y. Qi, W. Yang, F. Pan, J. Li, K. Xu, C. Wang, *J. Am. Chem. Soc.* **2017**, *139*, 18670–18680.
- [30] R. Jommongkol, S. Deebansok, J. Deng, Y. Zhu, R. Bouchal, O. Fontaine, *Small* **2024**, *20*, 2303945.
- [31] A. Ramos-Ballesteros, R. Gakhar, G. P. Horne, K. Iwamatsu, J. F. Wishart, S. M. Pimblott, J. A. LaVerne, *Phys. Chem. Chem. Phys.* **2021**, *23*, 10384–10394.
- [32] É. Bossé, L. Berthon, N. Zorz, J. Monget, C. Berthon, I. Bisel, S. Legand, P. Moisy, *Dalton Trans.* **2008**, 924–931.
- [33] B. J. Mincher, J. F. Wishart, *Solvent Extr. Ion Exch.* **2014**, *32*, 563–583.
- [34] P. Tarábek, A. Lisovskaya, D. M. Bartels, *J. Phys. Chem. B* **2019**, *123*, 10837–10849.
- [35] I. A. Shkrob, T. W. Marin, S. D. Chemerisov, J. F. Wishart, *J. Phys. Chem. B* **2011**, *115*, 3872–3888.
- [36] F. Neese, *WIREs Comput. Mol. Sci.* **2022**, *12*, e1606.
- [37] J. Klein, H. Khatabil, J.-C. Boisson, J. Contreras-García, J.-P. Piquemal, E. Hénon, *J. Phys. Chem. A* **2020**, *124*, 1850–1860.

- [38] T. Lu, F. Chen, *J. Comput. Chem.* **2012**, *33*, 580–592.
- [39] H. Fricke, E. J. Hart, in *Radiation Dosimetry*, Academic Press, New York, 1966.
- [40] Q. Chen, K. Schmidt-Rohr, *Macromolecules* **2004**, *37*, 5995–6003.
- [41] M. Puget, V. Shcherbakov, S. Denisov, P. Moreau, J.-P. Dognon, M. Mostafavi, S. Le Caër, *Chem. Eur. J.* **2021**, *27*, 8185–8194.
- [42] C. Ruckebusch, M. Sliwa, P. Pernot, A. de Juan, R. Tauler, *J. Photochem. Photobiol. C* **2012**, *13*, 1–27.
- [43] P. Pernot, **2018**, <https://doi.org/10.5281/zenodo.1064370>.
- [44] L. Martínez, R. Andrade, E. G. Birgin, J. M. Martínez, *J. Comput. Chem.* **2009**, *30*, 2157–2164.
- [45] S. Grimme, A. Hansen, S. Ehlert, J.-M. Mewes, *J. Chem. Phys.* **2021**, *154*, 064103.

Manuscript received: March 29, 2024

Revised manuscript received: May 15, 2024

Accepted manuscript online: May 28, 2024

Version of record online: July 16, 2024